

Accelerating the Discovery of Metastable IrO₂ for the Oxygen Evolution Reaction by the Self-Learning-Input Graph Neural Network

Jie Feng, Zhihao Dong, Yujin Ji,* and Youyong Li*



Cite This: *JACS Au* 2023, 3, 1131–1140



Read Online

ACCESS |

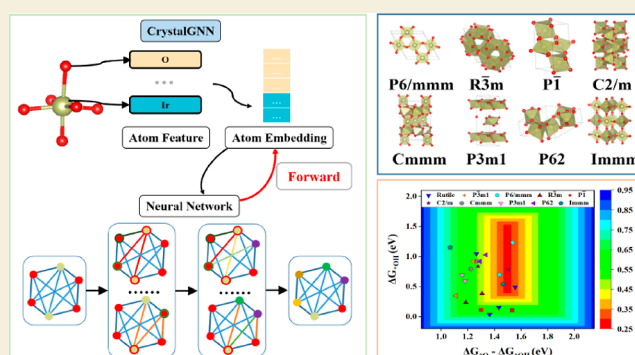
Metrics & More

Article Recommendations

Supporting Information

ABSTRACT: The discovery of active and stable catalysts for the oxygen evolution reaction (OER) is vital to improve water electrolysis. To date, rutile iridium dioxide IrO₂ is the only known OER catalyst in the acidic solution, while its poor activity restricts its practical viability. Herein, we propose a universal graph neural network, namely, CrystalGNN, and introduce a dynamic embedding layer to self-update atomic inputs during the training process. Based on this framework, we train a model to accurately predict the formation energies of 10,500 IrO₂ configurations and discover 8 unreported metastable phases, among which C2/m-IrO₂ and P62-IrO₂ are identified as excellent electrocatalysts to reach the theoretical OER overpotential limit at their most stable surfaces. Our self-learning-input CrystalGNN framework exhibits reliable accuracy, generalization, and transferring ability and successfully accelerates the bottom-up catalyst design of novel metastable IrO₂ to boost the OER activity.

KEYWORDS: graph neural network, metastable IrO₂, oxygen evolution reaction, crystal search



INTRODUCTION

In electrochemical water splitting, the four-electron oxygen evolution reaction (OER) is kinetically sluggish and restricts the overall efficiency for hydrogen production.^{1–3} To date, rutile IrO₂ is the only known OER catalyst with high stability in acidic solution;⁴ however, its practical application is to a large extent hindered by low OER activity.⁵ Much effort has been devoted to improving their catalytic activities, including heteroatom doping,^{6–8} morphology, surface modulation,^{9–13} exploring metastable allotropes,^{14,15} and so forth, among which metastable configurations are expected to achieve better catalytic performance due to their diversities of bond orders and active sites.^{16–18} For example, recently our synthesized 1T- and 3R-phase IrO₂ exhibited excellent OER activities and stabilities at the same time.^{14,15} Therefore, searching for metastable IrO₂ is an effective strategy to design highly efficient OER catalysts.

Although many crystal search techniques successfully promote the identification of unknown metastable structures, it remains a huge challenge to rapidly screen ideal candidates in the entire material space.^{19–23} As an emerging and state-of-art technology, machine learning (ML) has demonstrated great potential in accelerating crystal discovery,^{24–26} contributing to lower experimental costs and better bottom-up design protocols.^{27–30} Because crystals/molecules are usually non-Euclidean, graph neural networks (GNNs) have been

confirmed far beyond traditional ML methods and proposed as a well-suited deep learning protocol in predicting material properties, such as CGCNN,³¹ MEGNet,³² iCGCNN,³³ and GeoCGNN.³⁴ However, it should be noted that the information of these inputs is usually encoded by artificially selected atomic properties; in other words, the inputs among these ML frameworks require a case-by-case design, which leads to narrow applicability outside of their training scope.

In this work, we propose a universal GNN-based algorithm, named CrystalGNN, in which the only inputs for predicting material properties are the atomic number, bond length, and adjacent matrix in the crystal. To gain this aim, we introduce a dynamic embedding layer to accept the feedback of back-propagation during the training process, thereby the inter-atomic and intra-atomic correlation are self-captured adaptively along with the iteration of the neural network. It is found that our CrystalGNN framework can achieve reliable accuracy, generalization, and transferring ability with non-empirical

Received: December 30, 2022

Revised: March 16, 2023

Accepted: March 29, 2023

Published: April 11, 2023



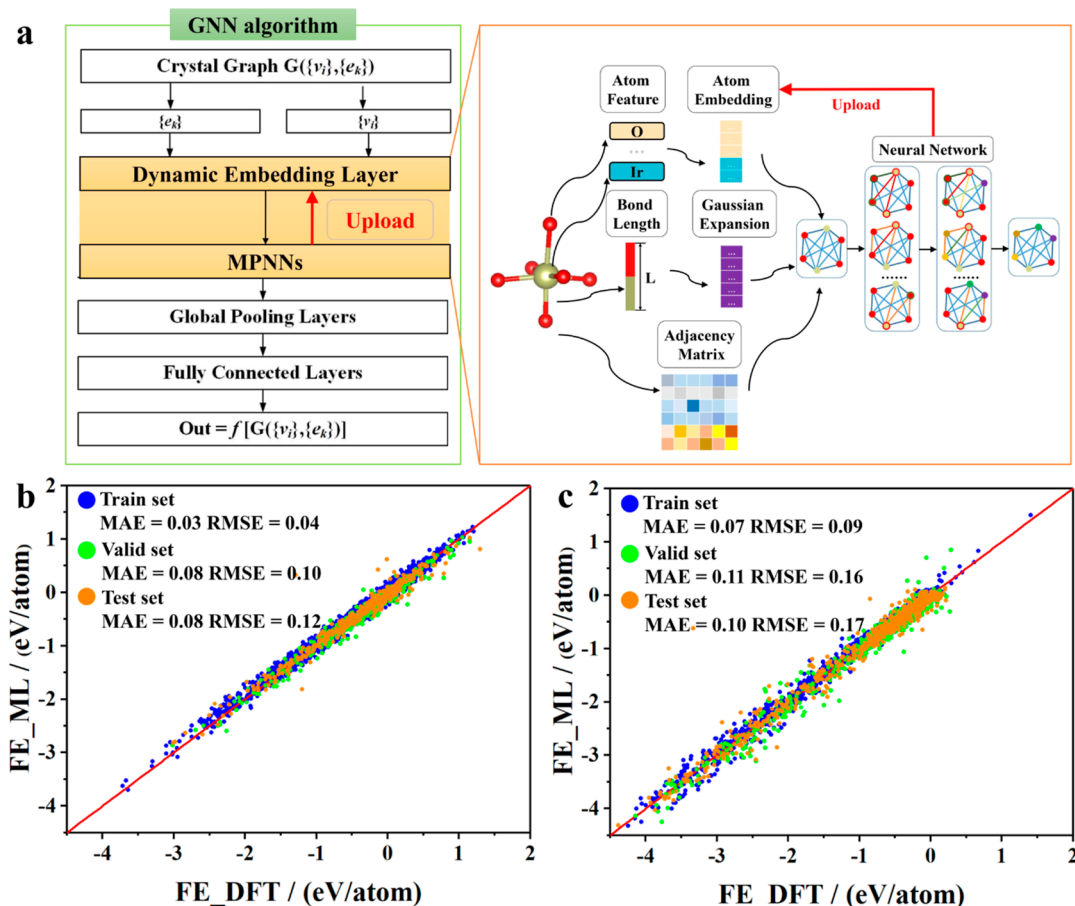


Figure 1. The framework and performance of CrystalGNN. (a) Framework of CrystalGNN and workflow of the dynamic embedding layer. The performance of CrystalGNN for predicting the formation energies (FE) of (b) two-dimensional materials in the C2DB data set and (c) bulk materials in the Materials Project data set.

inputs. We then utilize it to accelerate the exploration of metastable IrO_2 and search $\sim 10,000$ IrO_2 configurations, among which two kinds of novel metastable IrO_2 are identified with considerable OER stabilities and activities.

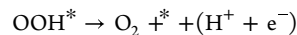
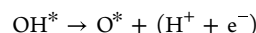
METHODS

Density Functional Theory Calculations

The IrO_2 structures are generated from CALYPSO^{23,35} and are optimized within the density functional theory (DFT) framework by the Vienna Ab initio Simulation Package (VASP).^{36–38} The generalized gradient approximation³⁹ of Perdew–Burke–Ernzerhof (GGA-PBE)⁴⁰ is applied to represent the exchange–correlation energy, and a cutoff energy of 400 eV is used. The energy convergence criterion is set to 10^{-4} eV and the force convergence criterion is set to $0.05 \text{ eV}\cdot\text{\AA}^{-1}$ for each atom. The Γ -centered k-point grids of $30/a \times 30/b \times 30/c$ and $30/a \times 30/b \times 1$ are chosen for bulk and slab calculations, respectively. For all slabs, a vacuum distance of 12 Å is added along the z direction, and the bottom layers are fixed, while the remaining layers are relaxed. To assess the kinetic and thermal stabilities of these metastable structures, we employ the finite displacement method to calculate the phonon dispersion via the PHONOPY program⁴¹ and perform 5 ps ab initio molecular dynamics (AIMD) simulations at 400 K under the NVT ensemble with a time step of 1.0 fs.

OER Reaction

The OER reaction under acidic conditions contains four intermediate steps as follows³



where * represents an active site on the clean surface and *OH, *O, and *OOH denote hydroxyl, oxo-, and hydroperoxide intermediates adsorbed on the surface, respectively.⁴²

According to the computational hydrogen electrode (CHE) model,⁴³ the chemical potential of the proton–electron pair can be expressed by the chemical potential of H_2 in the gas phase

$$G(\text{H}^+) + G(\text{e}^-) = \frac{1}{2}G(\text{H}_2) \quad (1)$$

The Gibbs free-energy change (ΔG_i) for every OER elementary steps is given as the difference between the initial and final states⁴⁴

$$\Delta G_i = \Delta E_i + \Delta \text{ZPE} - T\Delta S \quad (2)$$

where ΔE_i represents the energy difference between the reactant and product, ΔZPE represents changes in the zero-point energy, $T\Delta S$ represents changes in entropy, and T represents the temperature, which is set to 298.15 K. The zero-point energy and entropy can be calculated by the following formulas

$$\text{ZPE} = \sum_i \frac{1}{2}h\nu_i \quad (3)$$

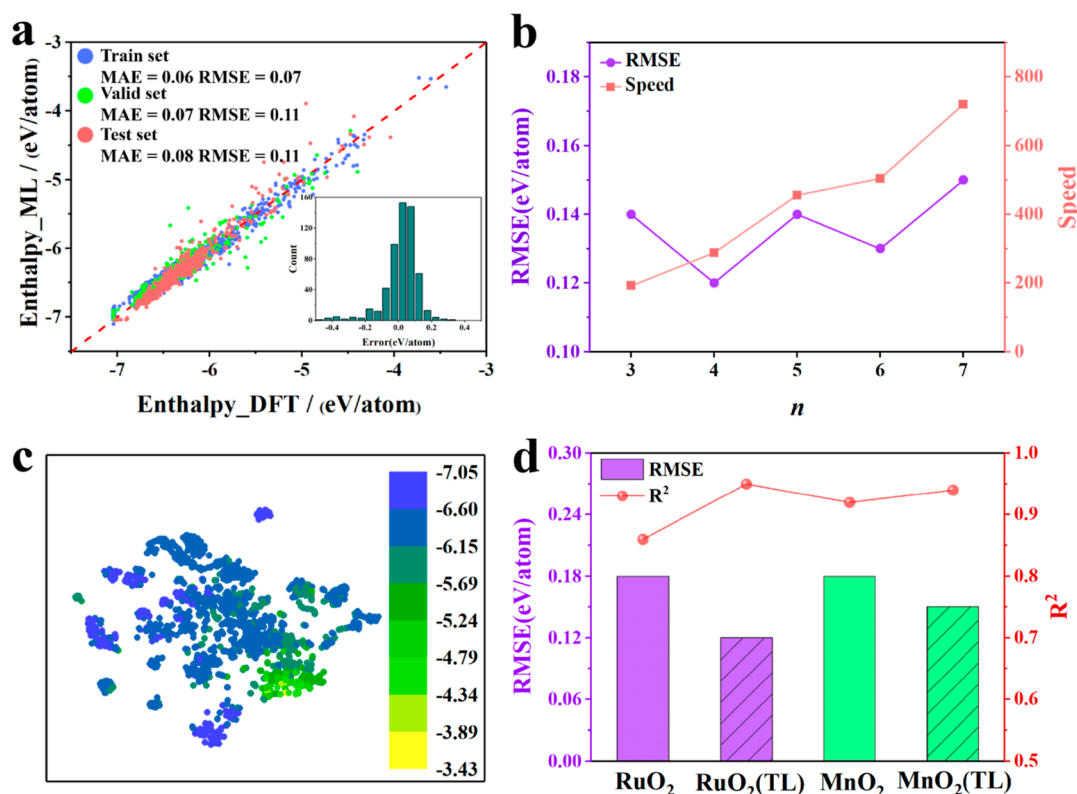


Figure 2. The results of the crystal structure search accelerated by machine learning. (a) Parity plots between predicted enthalpies and DFT-calculated enthalpies for IrO₂. Insets are histograms of the error distributions for the test set. (b) RMSE and the speed of prediction for IrO₂ with $n = 3, 4, 5, 6$ and 7 . (c) Visualization of graph-wide feature space of the t -distributed stochastic neighbor embedding (t -SNE) plot of the graph-level embedding from the output of the pooling layer. (d) RMSE and R^2 of prediction for RuO₂ and MnO₂ by the original data and transfer learning from IrO₂ data. The “TL” represents the model trained by transfer learning.

$$S = k_B \sum_i \left(\frac{h\nu_i}{k_B T \left(\exp\left(\frac{h\nu_i}{k_B T}\right) - 1 \right)} - \ln \left(1 - \exp\left(\frac{-h\nu_i}{k_B T}\right) \right) \right) \quad (4)$$

where h denotes the Planck's constant, k_B denotes the Boltzmann constant, and ν_i denotes the vibrational frequency.

The limiting potential of the OER is defined as the change in Gibbs free energy in the potential determining step (PDS), namely

$$U_{\text{limiting}} = \max\{\Delta G_i\} \quad (5)$$

and the overpotential of the OER reaction can be written as⁴²

$$\eta = \frac{U_{\text{limiting}}}{e} - 1.23 \quad (6)$$

where 1.23 V is the equilibrium potential for the OER. In addition, to avoid computational error for triplet oxygen, the free energy of O₂ is calculated from the experimental free energy of the OER reaction $\Delta G = -4.92$ eV.⁴³ The surface energy E_{sur} is calculated by

$$E_{\text{sur}} = \frac{(E_{\text{slab}} - N \cdot E_{\text{bulk}})}{2A} \quad (7)$$

where E_{slab} is the energy of the surface, E_{bulk} is the energy of the bulk, A is the surface area, and N is the number of IrO₂ units.

RESULTS

Framework of CrystalGNN Algorithm

As shown in Figure 1a, our proposed CrystalGNN is under the framework of the message passing mechanism,⁴⁵ including message passing layer, global pooling layer, and fully connected

layer. The crystal structure is normally encapsulated into graph data, whose nodes and edges correspond to crystal atoms and bonds. For the information of bonds, bond lengths less than a cutoff radius are chosen to reflect the connections between atoms, which are mathematically transformed into discrete eigenvectors $\{e_k\}$ by the Gaussian expansion. However, for the attributes of each atom $\{v_i\}$, there is no unified paradigm and their physiochemical properties are usually artificially selected to represent discrete atomic information by the one-hot encoding method,^{31,46–48} making these eigenvectors independent of each other. The main idea of our CrystalGNN is to encode the atomic attributes $\{v_i\}$ into a fixed-dimension dense vector $\{v'_i\}$ in a dynamic embedding layer and let it self-update to adaptively reflect the intra-atomic and inter-atomic correlation along with the iteration of the neural network, namely

$$v'_i = \omega v_i \quad (8)$$

where ω represents the initial coefficient. During the iteration of the neural network, the aggregation function f_{agg} is used to obtain the aggregated feature ω^t at the t -th iteration, and then ω^t is passed into an update function to obtain a new v'_i , namely

$$\omega^t = f_{\text{agg}}(\omega) \quad (9)$$

$$v'_i = \omega^t v'_i \quad (10)$$

Based on the f_{agg} to accept the feedback of backpropagation during the training process, the dynamic embedding layer will

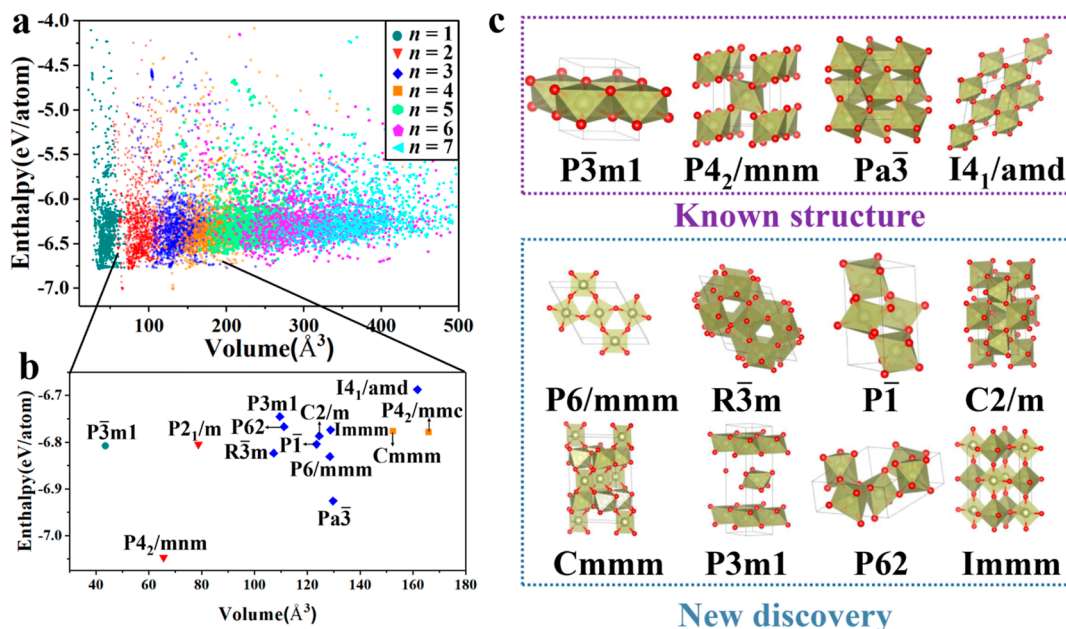


Figure 3. Summary of the crystal structure search by our framework. (a) Scatter diagram plots the volumes and enthalpies of the $\sim 10,000$ structures. (b) Selected low-energy region of the scatter diagram plots. (c) Selected stable structure in the low-energy region, in which the known structures are the stable phases synthesized in the experiment while the new discovery structures are the newly discovered with low enthalpies and dynamic stability.

automatically optimize the atomic information when the model reaches the best. The introduction of this embedding layer can make the initial atomic vectors dense and intrinsically related; therefore, only a single atomic number encoded into a 128-dimensional dense vector for every constituent atom is taken as the input, which is enough to obtain ideal accuracy for ML. (Supporting Information, Table S1). Details of our CrystalGNN framework can be accessed in Supporting Note, S1.

Accordingly, we evaluate the performance of our CrystalGNN framework in the prediction of the formation energies of crystal materials in the C2DB data set⁴⁹ and Materials Project data set.⁵⁰ It is found that the mean absolute errors (MAEs) for two-dimensional and bulk materials can reach 0.08 and 0.10 eV, which are comparable to the benchmark (0.05–0.2 eV) of other GNNs⁵¹ (Figure 1b,c). Specifically, we compare the performance of CrystalGNN and CGCNN in the regression task (predicting the formation energies, band gaps, and absolute energies) and the classification task (predicting the classifications of metal and semiconductor). The results demonstrate that the performance of CrystalGNN is comparable to that of CGCNN, and in some tasks, CrystalGNN may achieve better performance. (Supporting Information, Table S2).

In order to emphasize the advantage of the embedding layer, we decrease the inputs of CGCNN and find that the CGCNN deteriorates as the MAE increases from 0.11 to 0.16 eV/atom if only one atom feature is used, whereas the predicting accuracies of our CrystalGNN barely change when the number of atom features decreases. (Supporting Information, Figure S1). Our proposed CrystalGNN can maintain ideal accuracy regardless of which atom feature is selected, which is mainly attributed to the introduction of self-updated mechanism for the atom feature. This also confirms that our proposed CrystalGNN needs fewer inputs to obtain appropriate accuracy.

ML Workflow of Searching IrO₂

In the search for crystal structures, the number of IrO₂ formula units (n) in the crystal cell is a vital parameter, as a larger n means a more complex structure. At first, we screen the IrO₂ crystal space with $n = 1-2$ and for each n , 1500 initial structures are optimized. P4₂/mnm-IrO₂, namely, rutile phase (where the tag XXX in XXX-IrO₂ represents the space group of IrO₂), is selected as the most stable phase, which is consistent with the experimental results.^{4,52,53} However, due to their complex structures, the metastable I4₁/amd-IrO₂¹² and Pa $\bar{3}$ -IrO₂⁵⁴ successfully synthesized in experiments are missing, which motivates us to perform detailed structure searching for more unknown complex structures.

Next, we summarize these 3000 structures as the initial data set and employ CrystalGNN to train an ML model for enthalpy prediction. The performance of this ML model is shown in Figure 2a, in which the root mean square errors (RMSEs) are 0.07, 0.11, and 0.11 eV/atom for the training set, validation set, and test set, respectively. The inserted error distribution of the test set reflects that the deviations between DFT calculations and ML predictions are mostly located at 0–0.15 eV/atom ($\sim 90\%$), and only 10% of the error points are located at > 0.15 eV/atom. At this point, our proposed CrystalGNN achieves great accuracy for predicting the enthalpies of IrO₂ structures in the initial ML model.

Then, we conduct an exhaustive crystal structure search for complex structures, where n is set from 3 to 7 and for each n , 1500 structures are collected. To reflect the accuracy and efficiency of our framework, for each n , we illustrate the RMSE of the prediction and the ratio of the DFT-consumed time to ML-consumed time in Figure 2b. The RMSE value range from 0.12 to 0.15 eV/atom, whose performances are close to that of the initial model. We note that the more complex the structure is, the more computing power consumes, so when the value of n increases, the accelerating effect becomes more evident. Meanwhile, the prediction of IrO₂ crystals with $n = 3-7$ is still

Table 1. Space Group, Lattice Constant, Enthalpy, Ir–O Coordination Number, and Band Gap of the Four Known Structures and Eight Newly Discovered Structures of IrO₂^a

space group	<i>n</i>	<i>a</i>	<i>b</i>	<i>c</i>	enthalpy	Ir–O coordination	band gap
<i>P</i> $\bar{3}m1$	1	3.14	3.14	4.11	−6.81	6	1.94
<i>P</i> 4 ₂ / <i>mnm</i>	2	4.54	4.54	3.19	−7.05	6	0
<i>Pa</i> $\bar{3}$	4	4.94	4.94	4.94	−6.93	6	0.53
<i>I</i> 4 ₁ / <i>amd</i>	4	5.62	5.62	5.62	−6.69	6	0
<i>P</i> 6/ <i>mmm</i>	3	7.22	7.22	2.80	−6.83	4	1.04
<i>R</i> $\bar{3}m$	3	4.86	4.86	4.86	−6.82	6	0.52
<i>P</i> $\bar{1}$	3	3.18	4.42	7.36	−6.80	6	0.64
<i>C</i> 2/ <i>m</i>	3	5.23	8.39	4.36	−6.79	6	0.24
<i>C</i> <i>mmm</i>	3	10.36	7.14	3.08	−6.77	6, 4	0.29
<i>P</i> 3 <i>m</i> 1	3	3.14	3.14	12.74	−6.77	6	1.74
<i>P</i> 62	3	6.31	6.31	3.10	−6.75	6	1.00
<i>I</i> <i>mmm</i>	4	7.17	7.40	3.09	−6.78	6, 4	0

^a*n* represents the number of formula units in the simulation cell. *a*, *b*, and *c* represent the lattice constants. The enthalpies (eV) and band gap (eV) of these structures were obtained by DFT calculations.

accurate even though there are no known structures in the ML model, reflecting that our CrystalGNN has a good generalization ability and thus guarantees the efficiency and accuracy of exploring complex structures on the basis of simple structures. We visualize the output of the pooling layer with *t*-distributed stochastic neighbor embedding (*t*-SNE) in Figure 2c, whose close points in the same cluster are expected to share similarities in atomic structures and crystal configuration. This implies that our CrystalGNN can generate viable representations and group the crystals delineated by similar enthalpies. Because CrystalGNN has learned the structure and composition representations of simple IrO₂ phases, our model naturally presents good performance in complex phases.

Moreover, we also extend this framework to similar RuO₂ and MnO₂ systems because RuO₂ and MnO₂ are also reported to have high stability and activity in the OER.^{55–59} We apply transfer learning to improve the performance by training the data of RuO₂ and MnO₂ based on the IrO₂ models. As illustrated in Figure 2d, both the prediction accuracies and efficiencies for RuO₂ and MnO₂ models increase. It is worth noting that CrystalGNN also achieves high predicting accuracy (0.12 eV/atom for RuO₂ and 0.14 eV/atom for MnO₂) in Supporting Information, Table S3 and accelerates the efficiency of the crystal search in Supporting Information, Figures S2 and S3. Therefore, our CrystalGNN has an excellent ability of generalization and transfer learning, while maintaining accuracy.

Metastable IrO₂ Structures

After the exhaustive structure search of IrO₂, Figure 3a exhibits the distribution of the formation enthalpies for a total of 10,500 structures. For *n* = 1, the most stable structure is *P* $\bar{3}m1$ -IrO₂, named 1T-phase IrO₂, which has been recently synthesized.¹⁴ For *n* = 2 and *n* = 4, *P*4₂/*mnm*-IrO₂ is located at the minimum enthalpy as it is recognized as the most stable phase both experimentally and theoretically. For *n* = 4, *I*4₁/*amd*-IrO₂ and *Pa* $\bar{3}$ -IrO₂ are successfully searched. It is clear that the volumes of IrO₂ bulks expand with increasing parameter *n*, and there is a weak relationship between the enthalpy and volume. When *n* is increased to 5–7, the proportions of stable metastable IrO₂ decrease. Considering that the enthalpy (−6.69 eV/atom) of *I*4₁/*amd*-IrO₂ is the largest among four synthesized IrO₂ structures, we take it as a threshold and find 10 unreported IrO₂ phases (Figure 3b). Then, in order to further verify the thermo- and kinetic

stabilities of these new configurations, we also analyze their phonon spectra and 5 ps ab initio molecular dynamics. (Supporting Information, Figures S4 and S5). Finally, eight metastable IrO₂ candidates are confirmed without imaginary frequency and geometry distortion, which are promising for synthesis in experiments. Their relative formation enthalpies are as follows: *P*4₂/*mnm* < *Pa* $\bar{3}$ < *P*6/*mmm* < *R* $\bar{3}m$ < *P* $\bar{3}m1$ < *P* $\bar{1}$ < *C*2/*m* < *I**mmm* < *C**mmm* < *P*3*m*1 < *P*62 < *I*4₁/*amd*.

Figure 3c shows the geometric structures of eight novel metastable phases. *P*4₂/*mnm*-IrO₂ has a primitive cell of tetragonal configuration with the mixed edge- and corner-sharing octahedral, whereas *I*4₁/*amd*-IrO₂ is also in the tetragonal crystal system with the exclusively edge-sharing octahedral. *Pa* $\bar{3}$ -IrO₂, *P* $\bar{3}m1$ -IrO₂, *R* $\bar{3}m$ -IrO₂, and *P*3*m*1-IrO₂ all belong to the trigonal crystal system. The primitive cell of *R* $\bar{3}m$ -IrO₂ presents a compact edge-sharing octahedral. *P* $\bar{3}m1$ -IrO₂ and *P*3*m*1-IrO₂ have a two-dimensional configuration, which is structurally similar to 2D transition-metal dichalcogenides and their main difference is the layered stacking mode. *P*6/*mmm*-IrO₂ is a one-dimensional phase in the hexagonal system, whose Ir atoms and O atoms lie nearly in the same plane. *P* $\bar{1}$ -IrO₂, belonging to the triclinic system, consists of a nine-atom primitive cell with an exclusively corner-sharing octahedral. *C*2/*m*-IrO₂ has a monoclinic configuration, where the Ir atoms and O atoms form a mixed edge- and corner-sharing octahedral. *I**mmm*-IrO₂ and *C**mmm*-IrO₂ have similar structures as they are both orthorhombic but present varying degrees of connectivity. *P*62-IrO₂ falls within the hexagonal system, where one Ir atom and one O atom are located at the hexahedron face and another Ir atom and three O atoms located in the interior of the hexahedron. Overall, the Ir–O coordination numbers of all metastable phases are 4, 6, or a mixture of 4 and 6, which are common in other transition-metal dioxides.⁶⁰ IrO₂ prefers to construct an octahedral configuration, whose Ir atoms share more oxygen to maintain stoichiometry, resulting in a universal six-coordinated number. The Ir–O coordination numbers in *I**mmm*-IrO₂ and *C**mmm*-IrO₂ are both 4 and 6 due to the existence of oxygen vacancies. The planar configuration of *P*6/*mmm*-IrO₂ is accompanied by the special coordination number of 4.

Moreover, we also evaluate their band structures and find that *P*4₂/*mnm*-IrO₂, *I*4₁/*amd*-IrO₂, and *I**mmm*-IrO₂ present metallic properties without band gaps. *C*2/*m*-IrO₂ and *C**mmm*-IrO₂ are semiconductors with narrow band gaps of 0.24 and

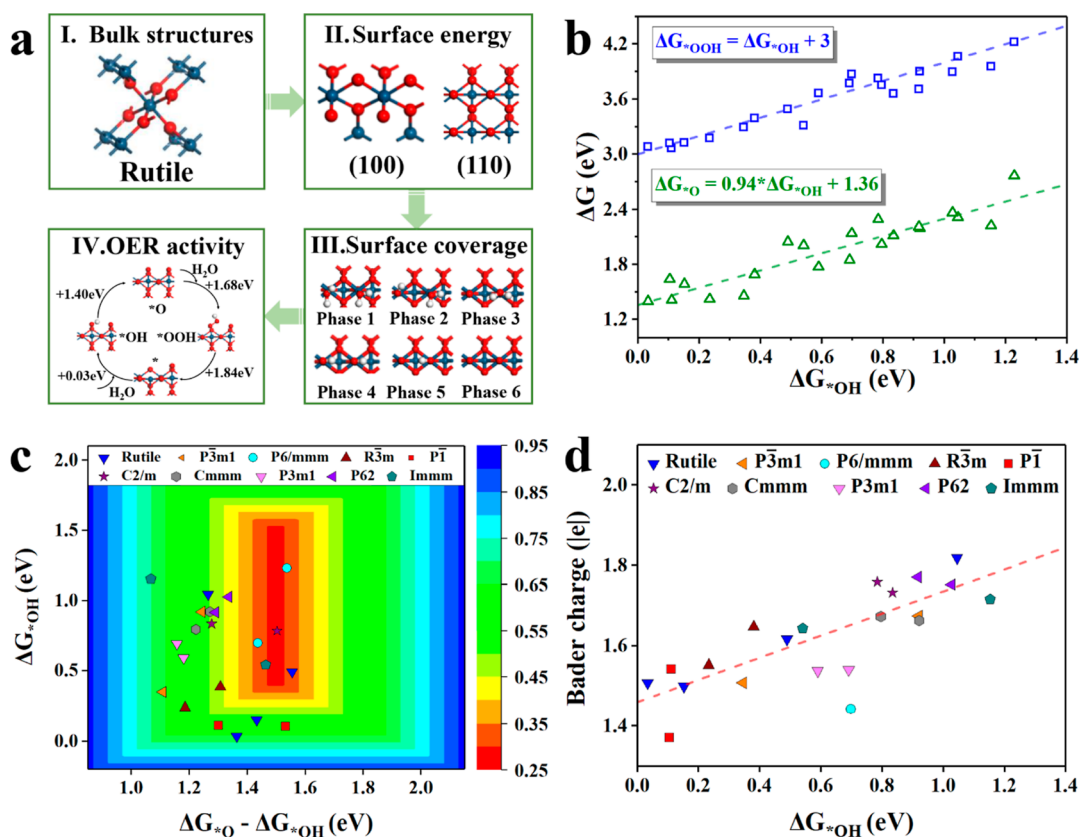


Figure 4. The OER activities of the metastable structures. (a) Scheme for computing the OER activities of metastable structures. (b) Scaling relationships of ΔG_{O^*} vs ΔG_{OH^*} and ΔG_{OOH^*} vs ΔG_{OH^*} . (c) Two-dimensional volcano plot of the OER overpotentials as a function of ΔG_{OH^*} and $\Delta G_{\text{O}^*} - \Delta G_{\text{OH}^*}$. (d) Relationship between Bader charge of the surface Ir atom and ΔG_{OH^*} .

0.29 eV, respectively. The band gaps of $P\bar{a}3\text{-IrO}_2$, $R\bar{3}m\text{-IrO}_2$, and $P\bar{1}\text{-IrO}_2$ are approximately 0.6 eV and the band gaps of $P6/mmm\text{-IrO}_2$ and $P62\text{-IrO}_2$ are approximately 1.0 eV while $P\bar{3}m1\text{-IrO}_2$ and $P3m1\text{-IrO}_2$ possess relatively wider band gaps of up to 1.94 and 1.74 eV, respectively. The basic information and physical properties of these eight novel phases are summarized in Table 1 and Supporting Information, Figure S6.

Screening of the OER Activities

Last but not least, we perform ab initio calculations to screen the OER activities of these eight metastable structures under the scheme of Figure 4a. For each metastable IrO_2 bulk, we cleave its six low-index (100), (010), (001), (110), (011), and (101) surfaces and compare their surface energies to determine the stable exposed surfaces. (Supporting Information, Table S4). Then, we choose the two most stable surfaces of each metastable IrO_2 and further analyze their surface Pourbaix diagrams to understand the equilibrium surface structures under the OER operating electrochemical potentials. (Supporting Information, Figure S7). Under an electrochemical potential of 1.5–2.0 V, it is found that the fully oxygen-terminated surfaces for all configurations possess the lowest thermodynamic potential and are selected to investigate the free energy evolutions of the four elementary reaction steps, including the O^* , OH^* , and OOH^* intermediates. In total, the OER activities of 22 surfaces are evaluated along the conventional adsorbate evolution mechanism. (Supporting Information, Table S5).

It is universally acknowledged that scaling relationships exist for the Gibbs free binding energies of the OER intermediates.^{42,61} The scaling relationships of ΔG_{O^*} vs ΔG_{OH^*} and

ΔG_{OOH^*} vs ΔG_{OH^*} are $\Delta G_{\text{O}^*} = 0.94\Delta G_{\text{OH}^*} + 1.36$ and $\Delta G_{\text{OOH}^*} = 1.00\Delta G_{\text{OH}^*} + 3.00$, respectively, in Figure 4b. The first-order relationships of ΔG_{OOH^*} and ΔG_{OH^*} are attributed to the single bond nature of *OH and *OOH on the active sites, which are in agreement with previous studies of OER catalyst materials.^{62,63} Based on the scaling relations, we straightforwardly summarize the volcanic OER overpotentials vs $\Delta G_{\text{O}^*} - \Delta G_{\text{OH}^*}$ in Figure 4c and Supporting Information, Figure S8. A moderate $\Delta G_{\text{O}^*} - \Delta G_{\text{OH}^*}$ of approximately 1.5 eV, or a ΔG_{OH^*} ranging from 0.5–1.5 eV, is linked to a low overpotential. Detailed information about the theoretical overpotentials and the PDSs is given in Supporting Information, Figure S9. It is found that the overpotential of rutile IrO_2 at the most stable (110) surface is 0.61 V with the PDS of $\text{OOH}^* \rightarrow \text{O}_2$, which corresponds to the previous theoretical and experimental outcomes.^{12,62,63} Although rutile IrO_2 (101) and (001) surfaces possess better OER performance with overpotentials of 0.53 and 0.33 V, respectively, the high surface energies of these two surfaces mean less exposed surface area for the OER. For a comparison, at the peak of the volcano is the (011) surface of $\text{C}2/m\text{-IrO}_2$, and the (100) surface of $\text{P}62\text{-IrO}_2$, whose overpotentials are close to 0.3 V at the most exposed surfaces. The PDSs of $\text{C}2/m\text{-IrO}_2$ (011) and $\text{P}62\text{-IrO}_2$ (100) surfaces are at $\text{O}^* \rightarrow \text{OOH}^*$ with overpotentials of 0.33 and 0.30 V, respectively. So, $\text{C}2/m\text{-IrO}_2$ and $\text{P}62\text{-IrO}_2$ are two promising OER catalyst materials as their most stable surfaces are more active than those of rutile IrO_2 .

Furthermore, in order to reveal the origin of this OER enhancement, we analyze the electronic properties and find

that the Bader charges of the Ir active sites are linearly dependent on ΔG_{OH^*} (Figure 4d). When the Bader charge of the Ir atom is approximately +1.4 |e|, its ΔG_{OH^*} is close to 0 eV, indicating a strong OH* adsorption. In contrast, there is weak OH* adsorption with ΔG_{OH^*} higher than 0.8 eV when the Bader charge is up to +1.8 |e|. The Bader charge of the Ir atom in rutile IrO₂ (110) is +1.51 |e|, which results in less oxidation of the Ir atom, thus making the OH* adsorption stronger. The experiments have confirmed that the closed characteristic of the (110) surface leads to the less oxidized Ir atom.^{64,65} The Bader charges of the Ir atom in *P3m1*-IrO₂, *P1*-IrO₂, and *P3m1*-IrO₂ range from +1.4|e| to +1.6|e|, accompanied by the strong OH* adsorptions. Therefore, their Ir atoms are less oxidized compared to the rest with better OER activities, which could be used to explain the poor catalytic performance of these metastable structures. On the contrary, the Bader charges of the Ir atom in *C2/m*-IrO₂ and *P62*-IrO₂ are within the range of +1.6|e|– +1.8|e|, which are observably higher than that in rutile IrO₂ (110), indicating more oxidation of the Ir atoms. The higher oxidation states of surface Ir atoms could be attributed to the local configurations of the metastable phases in which the Ir atoms and O atoms of monoclinic *C2/m*-IrO₂ form the compact mixed edge- and corner-sharing octahedral while the Ir atoms and O atoms of hexagonal *P62*-IrO₂ are located closely along the *z* direction and lead to better electron donation in the OER reaction compared to rutile IrO₂, corresponding to the appropriate adsorption of hydroxyl and easy desorption steps. Therefore, constructing specific metastable phases to modify the surface configurations and to increase the oxidation states of surface Ir atoms is a feasible strategy to improve the catalytic activity of IrO₂-based catalysts.

For the promising *C2/m*-IrO₂ and *P62*-IrO₂, we present more discussion on their OER mechanism and experimental prospect. Besides the conventional adsorbate evolving mechanism (AEM), the lattice oxygen mechanism (LOM) is competitive in the OER.⁶⁶ We compare the LOM and AEM on *C2/m*-IrO₂ and *P62*-IrO₂ in Supporting Information, Figure S10. It is found that the LOM on *C2/m*-IrO₂ is more energetic favorable OER pathway. The PDS of four-electron OER along the LOM is at *O → *H_{O-site} with the overpotentials of 0.27 and 0.22 V, which are lower than the AEM overpotentials of 0.31 and 0.32 V for (110) and (011) surfaces, respectively. In comparison, *P62*-IrO₂ still favors the AEM. The electronic-structure descriptor of oxygen p-band center is successful in describing catalytic activity trends for the OER in a variety of catalysts.^{67,68} Supporting Information, Figure S11 shows the projected density of states (DOS) distribution of the O 2p orbitals in *C2/m*-IrO₂ and *P62*-IrO₂. Compared with Rutile-IrO₂, the O 2p-band centers of *C2/m*-IrO₂ and *P62*-IrO₂ clearly shift closer to the Fermi level, corresponding to their higher oxidation states of surface Ir atoms. Meanwhile, there exists a clear linear correlation between the OER overpotentials and O 2p-band center, and a higher O 2p-band center corresponds to a better OER performance. For *C2/m*-IrO₂, and *P62*-IrO₂, their unique surface configurations contribute to the reasonable values of O 2p-band center, thus reaching the ideal OER activity. More importantly, in recent experimental report by Liao, et al.,⁶⁹ our experimental collaborators successfully synthesize monoclinic phase iridium oxide nanoribbon (IrO₂NR), which demonstrated better OER performance than the commercial Rutile IrO₂. Our proposed *C2/m*-IrO₂ shows several similarities with the experimental

IrO₂NR. Their space groups are the same *C2/m*, in which Ir and O atoms form the [Ir–O₆] octahedron with edge-sharing mode. The intrinsic catalytic activity of IrO₂NR exhibits low overpotential of 205 mV from the linear sweep voltammetry (LSV) curves, which are close to our calculated overpotentials of 0.27 V for (110) surface and 0.22 V for (011) surface, respectively. (Supporting Information, Figure S12).

CONCLUSIONS

In summary, we develop a universal self-learning-input deep learning framework, namely, the crystal graph neural network (CrystalGNN), for predicting the formation energies of bulk and two-dimensional materials and it exhibits high prediction accuracy, and excellent generalization and transferring abilities. The highlight of our CrystalGNN framework is the introduction of a dynamic embedding layer to self-update the atomic features adaptively along with the iteration of the neural network. Then, we realize an efficient workflow for accelerating the search for metastable IrO₂, where CrystalGNN learns from a simple structure data set to accurately predict the properties of complex IrO₂ structures. Under this workflow, we discover eight unreported metastable IrO₂ phases with enough kinetic and thermodynamic stabilities, which are promising for synthesis in experiments. Meanwhile, two metastable IrO₂ with the space groups of *C2/m* and *P62* are confirmed as distinguished OER electrocatalysts because the theoretical OER overpotentials at their most stable exposed surfaces are much lower than the benchmarked rutile IrO₂ and reach the theoretical volcanic limit. Their outstanding OER enhancement originates from the increasing oxidation states of surface Ir atoms. Our work not only proposes a new deep learning GNN framework for rapid crystal structure search but also successfully identifies two promising metastable IrO₂, which provides a targeted guideline for improving OER catalyst materials.

ASSOCIATED CONTENT

Supporting Information

The Supporting Information is available free of charge at <https://pubs.acs.org/doi/10.1021/jacsau.2c00709>.

Detail introduction of CrystalGNN, hyperparameters of the model, performance of CrystalGNN, phonon spectra, molecular dynamics, and band structure of newly discovered structures, OER activity of newly discovered structures, comparison of OER mechanism, density of states, similarities between the experimental IrO₂NR and our proposed *C2/m*-IrO₂, CrystalGNN, is open-source and available at <https://github.com/Austin6035>, and data sets generated during the current study (PDF)

AUTHOR INFORMATION

Corresponding Authors

Yujin Ji – Institute of Functional Nano & Soft Materials (FUNSOM), Jiangsu Key Laboratory for Carbon-Based Functional Materials & Devices, Soochow University, Suzhou, Jiangsu 215123, China; orcid.org/0000-0003-3177-2073; Email: yjji@suda.edu.cn

Youyong Li – Institute of Functional Nano & Soft Materials (FUNSOM), Jiangsu Key Laboratory for Carbon-Based Functional Materials & Devices, Soochow University, Suzhou,

Jiangsu 215123, China; Macao Institute of Materials Science and Engineering, Macau University of Science and Technology, Taipa 999078, China; orcid.org/0000-0002-5248-2756; Email: yyli@suda.edu.cn

Authors

Jie Feng – Institute of Functional Nano & Soft Materials (FUNSOM), Jiangsu Key Laboratory for Carbon-Based Functional Materials & Devices, Soochow University, Suzhou, Jiangsu 215123, China

Zhihao Dong – Institute of Functional Nano & Soft Materials (FUNSOM), Jiangsu Key Laboratory for Carbon-Based Functional Materials & Devices, Soochow University, Suzhou, Jiangsu 215123, China

Complete contact information is available at: <https://pubs.acs.org/10.1021/jacsau.2c00709>

Author Contributions

J.F., Z.D., and Y.J. completed the machine learning model. J.F. and Y.J. constructed the atomistic models and performed density functional calculations. Y.J. and Y.L. conceptualized and supervised this work. All the authors were involved in the drafting of the manuscript. CRediT: **Jie Feng** data curation, formal analysis, investigation, methodology, visualization, writing-original draft, writing-review & editing; **Zhihao Dong** data curation, formal analysis, investigation, methodology, writing-original draft, writing-review & editing; **Yujin Ji** conceptualization, data curation, formal analysis, investigation, methodology, project administration, supervision, writing-original draft, writing-review & editing; **Youyong Li** conceptualization, project administration, software, supervision, writing-original draft, writing-review & editing.

Notes

The authors declare no competing financial interest.

ACKNOWLEDGMENTS

This work was supported by National key research and development program of China (Grants no. 2022YFA1503100), the Natural Science Foundation of Jiangsu Province (BZ2020011), National Natural Science Foundation of China (Grants no. 22173067), the Science and Technology Development Fund, Macau SAR (FDCT no. 0052/2021/A), Collaborative Innovation Center of Suzhou Nano Science & Technology, the Priority Academic Program Development of Jiangsu Higher Education Institutions (PAPD), the 111 Project, and Joint International Research Laboratory of Carbon-Based Functional Materials and Devices.

REFERENCES

- (1) Li, L.; Wang, P.; Shao, Q.; Huang, X. Metallic Nanostructures with Low Dimensionality for Electrochemical Water Splitting. *Chem. Soc. Rev.* **2020**, *49*, 3072–3106.
- (2) Grimaud, A.; Diaz-Morales, O.; Han, B.; Hong, W. T.; Lee, Y.-L.; Giordano, L.; Stoerzinger, K. A.; Koper, M. T.; Shao-Horn, Y. Activating Lattice Oxygen Redox Reactions in Metal Oxides to Catalyze Oxygen Evolution. *Nat. Chem.* **2017**, *9*, 457–465.
- (3) Rossmeis, J.; Qu, Z.-W.; Zhu, H.; Kroes, G.-J.; Nørskov, J. K. Electrolysis of Water on Oxide Surfaces. *J. Electroanal. Chem.* **2007**, *607*, 83–89.
- (4) Lee, Y.; Suntivich, J.; May, K. J.; Perry, E. E.; Shao-Horn, Y. Synthesis and Activities of Rutile IrO₂ and RuO₂ Nanoparticles for Oxygen Evolution in Acid and Alkaline Solutions. *J. Phys. Chem. Lett.* **2012**, *3*, 399–404.

(5) Kibsgaard, J.; Chorkendorff, I. Considerations for the Scaling-up of Water Splitting Catalysts. *Nat. Energy* **2019**, *4*, 430–433.

(6) Wang, Y.; Zhang, L.; Yin, K.; Zhang, J.; Gao, H.; Liu, N.; Peng, Z.; Zhang, Z. Nanoporous Iridium-Based Alloy Nanowires as Highly Efficient Electrocatalysts toward Acidic Oxygen Evolution Reaction. *ACS Appl. Mater. Inter.* **2019**, *11*, 39728–39736.

(7) Nong, H. N.; Reier, T.; Oh, H.-S.; Glich, M.; Paciok, P.; Vu, T. H. T.; Teschner, D.; Heggen, M.; Petkov, V.; Schlögl, R.; et al. A Unique Oxygen Ligand Environment Facilitates Water Oxidation in Hole-Doped Irniox Core–Shell Electrocatalysts. *Nat. Catal.* **2018**, *1*, 841–851.

(8) Choi, S.; Park, J.; Kabiraz, M. K.; Hong, Y.; Kwon, T.; Kim, T.; Oh, A.; Baik, H.; Lee, M.; Paek, S. M.; et al. Pt Dopant: Controlling the Ir Oxidation States toward Efficient and Durable Oxygen Evolution Reaction in Acidic Media. *Adv. Funct. Mater.* **2020**, *30*, 2003935.

(9) Cui, Z.; Qi, R. First-Principles Simulation of Oxygen Evolution Reaction (Oer) Catalytic Performance of IrO₂ Bulk-Like Structures: Nanosphere, Nanowire and Nanotube. *Appl. Surf. Sci.* **2021**, *554*, 149591.

(10) Gao, J.; Xu, C.-Q.; Hung, S.-F.; Liu, W.; Cai, W.; Zeng, Z.; Jia, C.; Chen, H. M.; Xiao, H.; Li, J.; et al. Breaking Long-Range Order in Iridium Oxide by Alkali Ion for Efficient Water Oxidation. *J. Am. Chem. Soc.* **2019**, *141*, 3014–3023.

(11) Kim, Y.-T.; Lopes, P. P.; Park, S.; Lee, A.; Lim, J.; Lee, H.; Back, S.; Jung, Y.; Danilovic, N.; Stamenkovic, V.; et al. Balancing Activity, Stability and Conductivity of Nanoporous Core-Shell Iridium/Iridium Oxide Oxygen Evolution Catalysts. *Nat. Commun.* **2017**, *8*, 1449–1458.

(12) Seitz, L. C.; Dickens, C. F.; Nishio, K.; Hikita, Y.; Montoya, J.; Doyle, A.; Kirk, C.; Vojvodic, A.; Hwang, H. Y.; Nørskov, J. K.; et al. A highly active and stable IrO_x/SrIrO₃ catalyst for the oxygen evolution reaction. *Science* **2016**, *353*, 1011–1014.

(13) Yang, L.; Yu, G.; Ai, X.; Yan, W.; Duan, H.; Chen, W.; Li, X.; Wang, T.; Zhang, C.; Huang, X.; et al. Efficient Oxygen Evolution Electrocatalysis in Acid by a Perovskite with Face-Sharing IrO₆ Octahedral Dimers. *Nat. Commun.* **2018**, *9*, 5236–5239.

(14) Dang, Q.; Lin, H.; Fan, Z.; Ma, L.; Shao, Q.; Ji, Y.; Zheng, F.; Geng, S.; Yang, S.-Z.; Kong, N.; et al. Iridium Metallene Oxide for Acidic Oxygen Evolution Catalysis. *Nat. Commun.* **2021**, *12*, 6007–6010.

(15) Fan, Z.; Ji, Y.; Shao, Q.; Geng, S.; Zhu, W.; Liu, Y.; Liao, F.; Hu, Z.; Chang, Y.-C.; Pao, C.-W.; et al. Extraordinary Acidic Oxygen Evolution on New Phase 3R-Iridium Oxide. *Joule* **2021**, *5*, 3221–3234.

(16) Tan, X.; Geng, S.; Ji, Y.; Shao, Q.; Zhu, T.; Wang, P.; Li, Y.; Huang, X. Closest Packing Polymorphism Interfaced Metastable Transition Metal for Efficient Hydrogen Evolution. *Adv. Mater.* **2020**, *32*, 2002857.

(17) Reed, J.; Ceder, G. Role of Electronic Structure in the Susceptibility of Metastable Transition-Metal Oxide Structures to Transformation. *Chem. Rev.* **2004**, *35*, 4513–4534.

(18) Flores, R. A.; Paolucci, C.; Winther, K. T.; Jain, A.; Torres, J. A. G.; Aykol, M.; Montoya, J.; Nørskov, J. K.; Bajdich, M.; Bligaard, T. Active Learning Accelerated Discovery of Stable Iridium Oxide Polymorphs for the Oxygen Evolution Reaction. *Chem. Mater.* **2020**, *32*, 5854–5863.

(19) Zhao, J.; Shi, R.; Sai, L.; Huang, X.; Su, Y. Comprehensive Genetic Algorithm for ab Initio Global Optimisation of Clusters. *Mol. Simulat.* **2016**, *42*, 809–819.

(20) Lonie, D. C.; Zurek, E. Xtalopt: An Open-Source Evolutionary Algorithm for Crystal Structure Prediction. *Comput. Phys. Commun.* **2011**, *182*, 372–387.

(21) Falls, Z.; Avery, P.; Wang, X.; Hilleke, K. P.; Zurek, E. The Xtalopt Evolutionary Algorithm for Crystal Structure Prediction. *J. Phys. Chem. C* **2020**, *125*, 1601–1620.

(22) Glass, C. W.; Oganov, A. R.; Hansen, N. Uspex—Evolutionary Crystal Structure Prediction. *Comput. Phys. Commun.* **2006**, *175*, 713–720.

- (23) Wang, Y.; Lv, J.; Zhu, L.; Ma, Y. Crystal Structure Prediction Via Particle-Swarm Optimization. *Phys. Rev. B* **2010**, *82*, 094116.
- (24) Tong, Q.; Gao, P.; Liu, H.; Xie, Y.; Lv, J.; Wang, Y.; Zhao, J. Combining Machine Learning Potential and Structure Prediction for Accelerated Materials Design and Discovery. *J. Phys. Chem. Lett.* **2020**, *11*, 8710–8720.
- (25) Musa, E.; Doherty, F.; Goldsmith, B. R. Accelerating the Structure Search of Catalysts with Machine Learning. *Curr. Opin. Chem. Eng.* **2022**, *35*, 100771.
- (26) Ryan, K.; Lengyel, J.; Shatruck, M. Crystal Structure Prediction Via Deep Learning. *J. Am. Chem. Soc.* **2018**, *140*, 10158–10168.
- (27) Mansouri Tehrani, A.; Oliynyk, A. O.; Parry, M.; Rizvi, Z.; Couper, S.; Lin, F.; Miyagi, L.; Sparks, T. D.; Brgoch, J. Machine Learning Directed Search for Ultracompressible, Superhard Materials. *J. Am. Chem. Soc.* **2018**, *140*, 9844–9853.
- (28) Oliynyk, A. O.; Antono, E.; Sparks, T. D.; Ghadbeigi, L.; Gaultois, M. W.; Meredig, B.; Mar, A. High-Throughput Machine-Learning-Driven Synthesis of Full-Heusler Compounds. *Chem. Mater.* **2016**, *28*, 7324–7331.
- (29) Witman, M.; Ek, G.; Ling, S.; Chames, J.; Agarwal, S.; Wong, J.; Allendorf, M. D.; Sahlberg, M.; Stavila, V. Data-Driven Discovery and Synthesis of High Entropy Alloy Hydrides with Targeted Thermodynamic Stability. *Chem. Mater.* **2021**, *33*, 4067–4076.
- (30) Singstock, N. R.; Ortiz-Rodríguez, J. C.; Perryman, J. T.; Sutton, C.; Velázquez, J. M.; Musgrave, C. B. Machine Learning Guided Synthesis of Multinary Chevrel Phase Chalcogenides. *J. Am. Chem. Soc.* **2021**, *143*, 9113–9122.
- (31) Xie, T.; Grossman, J. C. Crystal Graph Convolutional Neural Networks for an Accurate and Interpretable Prediction of Material Properties. *Phys. Rev. Lett.* **2018**, *120*, 145301.
- (32) Chen, C.; Ye, W.; Zuo, Y.; Zheng, C.; Ong, S. P. Graph Networks as a Universal Machine Learning Framework for Molecules and Crystals. *Chem. Mater.* **2019**, *31*, 3564–3572.
- (33) Park, C. W.; Wolverton, C. Developing an Improved Crystal Graph Convolutional Neural Network Framework for Accelerated Materials Discovery. *Phys. Rev. Mater.* **2020**, *4*, 063801.
- (34) Cheng, J.; Zhang, C.; Dong, L. A Geometric-Information-Enhanced Crystal Graph Network for Predicting Properties of Materials. *Communications Materials* **2021**, *2*, 92–111.
- (35) Wang, Y.; Lv, J.; Zhu, L.; Ma, Y. Calypso: A Method for Crystal Structure Prediction. *Comput. Phys. Commun.* **2012**, *183*, 2063–2070.
- (36) Kresse, G.; Furthmüller, J. Efficient Iterative Schemes for Ab Initio Total-Energy Calculations Using a Plane-Wave Basis Set. *Phys. Rev. B* **1996**, *54*, 11169–11186.
- (37) Kresse, G.; Furthmüller, J. Efficiency of Ab-Initio Total Energy Calculations for Metals and Semiconductors Using a Plane-Wave Basis Set. *Comp. Mater. Sci.* **1996**, *6*, 15–50.
- (38) Hafner, J. Ab-Initio Simulations of Materials Using Vasp: Density-Functional Theory and Beyond. *J. Comput. Chem.* **2008**, *29*, 2044–2078.
- (39) Blöchl, P. E. Projector Augmented-Wave Method. *Phys. Rev. B* **1994**, *50*, 17953–17979.
- (40) Perdew, J. P.; Burke, K.; Ernzerhof, M. Generalized Gradient Approximation Made Simple. *Phys. Rev. Lett.* **1996**, *77*, 3865–3868.
- (41) Togo, A.; Oba, F.; Tanaka, I. First-Principles Calculations of the Ferroelastic Transition between Rutile-Type and CaCl₂-Type SiO₂ at High Pressures. *Phys. Rev. B* **2008**, *78*, 134106.
- (42) Man, I. C.; Su, H. Y.; Calle-Vallejo, F.; Hansen, H. A.; Martínez, J. I.; Inoglu, N. G.; Kitchin, J.; Jaramillo, T. F.; Nørskov, J. K.; Rossmeisl, J. Universality in Oxygen Evolution Electrocatalysis on Oxide Surfaces. *ChemCatChem* **2011**, *3*, 1159–1165.
- (43) Nørskov, J. K.; Rossmeisl, J.; Logadottir, A.; Lindqvist, L.; Kitchin, J. R.; Bligaard, T.; Jonsson, H. Origin of the Overpotential for Oxygen Reduction at a Fuel-Cell Cathode. *J. Phys. Chem. B* **2004**, *108*, 17886–17892.
- (44) Li, M.; Zhang, L.; Xu, Q.; Niu, J.; Xia, Z. N-Doped Graphene as Catalysts for Oxygen Reduction and Oxygen Evolution Reactions: Theoretical Considerations. *J. Catal.* **2014**, *314*, 66–72.
- (45) Gilmer, J.; Schoenholz, S. S.; Riley, P. F.; Vinyals, O.; Dahl, G. E. *Neural Message Passing for Quantum Chemistry*; International conference on machine learning, PMLR, 2017, pp 1263–1272.
- (46) Choudhary, K.; DeCost, B. Atomistic Line Graph Neural Network for Improved Materials Property Predictions. *npj Comput. Mater.* **2021**, *7*, 185–188.
- (47) Karamad, M.; Magar, R.; Shi, Y.; Siahrostami, S.; Gates, I. D.; Barati Farimani, A. Orbital Graph Convolutional Neural Network for Material Property Prediction. *Phys. Rev. Mater.* **2020**, *4*, 093801.
- (48) Wang, B.; Fan, Q.; Yue, Y. Study of Crystal Properties Based on Attention Mechanism and Crystal Graph Convolutional Neural Network. *J. Phys.: Condens. Matter* **2022**, *34*, 195901.
- (49) Haastруп, S.; Strange, M.; Pandey, M.; Deilmann, T.; Schmidt, P. S.; Hinsche, N. F.; Gjerding, M. N.; Torelli, D.; Larsen, P. M.; Riis-Jensen, A. C.; et al. The Computational 2d Materials Database: High-Throughput Modeling and Discovery of Atomically Thin Crystals. *2D Mater.* **2018**, *5*, 042002.
- (50) Jain, A.; Ong, S. P.; Hautier, G.; Chen, W.; Richards, W. D.; Dacek, S.; Cholia, S.; Gunter, D.; Skinner, D.; Ceder, G.; et al. Commentary: The Materials Project: A Materials Genome Approach to Accelerating Materials Innovation. *APL Mater.* **2013**, *1*, 011002.
- (51) Fung, V.; Zhang, J.; Juarez, E.; Sumpter, B. G. Benchmarking Graph Neural Networks for Materials Chemistry. *npj Comput. Mater.* **2021**, *7*, 84–88.
- (52) Geiger, S.; Kasian, O.; Ledendecker, M.; Pizzutillo, E.; Mingers, A. M.; Fu, W. T.; Diaz-Morales, O.; Li, Z.; Oellers, T.; Fruchter, L.; et al. The Stability Number as a Metric for Electrocatalyst Stability Benchmarking. *Nat. Catal.* **2018**, *1*, 508–515.
- (53) Kasian, O.; Geiger, S.; Li, T.; Grote, J.-P.; Schweinar, K.; Zhang, S.; Scheu, C.; Raabe, D.; Cherevko, S.; Gault, B.; et al. Degradation of Iridium Oxides Via Oxygen Evolution from the Lattice: Correlating Atomic Scale Structure with Reaction Mechanisms. *Energy Environ. Sci.* **2019**, *12*, 3548–3555.
- (54) Ono, S.; Kikegawa, T.; Ohishi, Y. High-Pressure and High-Temperature Synthesis of a Cubic IrO₂ Polymorph. *Physica B* **2005**, *363*, 140–145.
- (55) Lee, Y.; Suntivich, J.; May, K. J.; Perry, E. E.; Shao-Horn, Y. Synthesis and Activities of Rutile IrO₂ and RuO₂ Nanoparticles for Oxygen Evolution in Acid and Alkaline Solutions. *J. Phys. Chem. Lett.* **2012**, *3*, 399–404.
- (56) Kuo, D.-Y.; Paik, H.; Kloppenburg, J.; Faeth, B.; Shen, K. M.; Schlom, D. G.; Hautier, G.; Suntivich, J. Measurements of Oxygen Electroadsorption Energies and Oxygen Evolution Reaction on RuO₂ (110): A Discussion of the Sabatier Principle and Its Role in Electrocatalysis. *J. Am. Chem. Soc.* **2018**, *140*, 17597–17605.
- (57) Stoerzinger, K. A.; Diaz-Morales, O.; Kolb, M.; Rao, R. R.; Frydendal, R.; Qiao, L.; Wang, X. R.; Halck, N. B.; Rossmeisl, J.; Hansen, H. A.; et al. Orientation-Dependent Oxygen Evolution on RuO₂ without Lattice Exchange. *ACS Energy Lett* **2017**, *2*, 876–881.
- (58) Fang, Y.-H.; Liu, Z.-P. Mechanism and Tafel Lines of Electro-Oxidation of Water to Oxygen on RuO₂ (110). *J. Am. Chem. Soc.* **2010**, *132*, 18214–18222.
- (59) Zhao, Y.; Chang, C.; Teng, F.; Zhao, Y.; Chen, G.; Shi, R.; Waterhouse, G. I.; Huang, W.; Zhang, T. Defect-Engineered Ultrathin Δ -MnO₂ Nanosheet Arrays as Bifunctional Electrodes for Efficient Overall Water Splitting. *Adv. Energy Mater.* **2017**, *7*, 1700005.
- (60) Waroquiers, D.; Gonze, X.; Rignanese, G.-M.; Welker-Nieuwoudt, C.; Rosowski, F.; Göbel, M.; Schenk, S.; Degelmann, P.; André, R.; Glaum, R.; et al. Statistical Analysis of Coordination Environments in Oxides. *Chem. Mater.* **2017**, *29*, 8346–8360.
- (61) Koper, M. Thermodynamic Theory of Multi-Electron Transfer Reactions: Implications for Electrocatalysis. *J. Electroanal. Chem.* **2011**, *660*, 254–260.
- (62) Back, S.; Tran, K.; Ulissi, Z. W. Toward a Design of Active Oxygen Evolution Catalysts: Insights from Automated Density Functional Theory Calculations and Machine Learning. *Acs Catal* **2019**, *9*, 7651–7659.

(63) Gunasooriya, G.; Nørskov, J. K. Analysis of Acid-Stable and Active Oxides for the Oxygen Evolution Reaction. *ACS Energy Lett.* **2020**, *5*, 3778–3787.

(64) Stoerzinger, K. A.; Qiao, L.; Biegalski, M. D.; Shao-Horn, Y. Orientation-Dependent Oxygen Evolution Activities of Rutile IrO₂ and RuO₂. *J. Phys. Chem. Lett.* **2014**, *5*, 1636–1641.

(65) Guerrini, E.; Trasatti, S. Recent Developments in Understanding Factors of Electrocatalysis. *Russ. J. Electrochem.* **2006**, *42*, 1017–1025.

(66) Zagalskaya, A.; Alexandrov, V. Role of Defects in the Interplay between Adsorbate Evolving and Lattice Oxygen Mechanisms of the Oxygen Evolution Reaction in RuO₂ and IrO₂. *ACS Catal.* **2020**, *10*, 3650–3657.

(67) Grimaud, A.; May, K. J.; Carlton, C. E.; Lee, Y.-L.; Risch, M.; Hong, W. T.; Zhou, J.; Shao-Horn, Y. Double Perovskites as a Family of Highly Active Catalysts for Oxygen Evolution in Alkaline Solution. *Nat. Commun.* **2013**, *4*, 2439.

(68) Grimaud, A.; Diaz-Morales, O.; Han, B.; Hong, W. T.; Lee, Y.-L.; Giordano, L.; Stoerzinger, K. A.; Koper, M. T.; Shao-Horn, Y. Activating Lattice Oxygen Redox Reactions in Metal Oxides to Catalyze Oxygen Evolution. *Nat. Chem.* **2017**, *9*, 457–465.

(69) Liao, F.; Yin, K.; Ji, Y.; Zhu, W.; Fan, Z.; Li, Y.; Zhong, J.; Shao, M.; Kang, Z.; Shao, Q. Iridium oxide nanoribbons with metastable monoclinic phase for highly efficient electrocatalytic oxygen evolution. *Nat. Commun.* **2023**, *14*, 1248.